Offset-Free Optimal Control of Cascaded H-Bridge Converters Based on a Kalman Filter Harmonic Compensator

Pablo Poblete, *Member, IEEE*, Ricardo P. Aguilera, *Member, IEEE*, Javier Pereda, *Senior Member, IEEE*, Rodrigo H. Cuzmar, Abraham M. Alcaide, *Member, IEEE*, Dylan Dah-Chuan Lu, *Senior Member, IEEE*, Yam Prasad Siwakoti, *Senior Member, IEEE*, and Pablo Acuna, *Member, IEEE*

***Abstract*—Cascaded H-bridge (CHB) converters are suitable candidates for numerous applications, including electrical drives, static synchronous compensators, and battery energy storage inverters. Optimal control strategies for CHB converters have attracted significant interest in recent decades due to their flexibility in including multiple control objectives and their simple design process. However, the steady-state performance of these control strategies deteriorates if the CHB converter model has parameter mismatches and/or the submodule (SM) capacitor voltage ripples are not measured. This work proposes a Kalman filter (KF) based strategy to eliminate the steady-state error and undesired low-frequency harmonic components in the CHB converter output currents. The proposed KF strategy estimates the instantaneous arm voltage harmonics representing the converter modeling errors and unaccounted disturbances. Then, these estimated voltage harmonics are used to improve the arm current predictions and obtain a compensation term for the steady-state arm voltage references to be used by the optimal control strategy. Experimental results for three different optimal control schemes are provided for a three-phase CHB converter with nine SMs to confirm the effectiveness of the proposed KF strategy.**

***Index Terms*—Cascaded H-Bridge (CHB), Kalman filtering, predictive control.**

Received 27 May 2024; revised 25 August 2024; accepted 29 September 2024. Date of publication 2 October 2024; date of current version 12 December 2024. This work was supported in part by the Australian Government through the Australian Research Council under Discovery Project DP240102646 and in part by ANID through FONDAP 1523A0006 SERC-Chile and Fondecyt Regular under Grant 1231265 and Grant 122098. Recommended for publication by Associate Editor L. Peng. *(Corresponding author: Pablo Poblete.)*

Pablo Poblete and Rodrigo H. Cuzmar are with the Department of Electrical Engineering, Pontificia Universidad Católica de Chile, Santiago 7820436, Chile, and also with the School of Electrical and Data Engineering, University of Technology Sydney, Broadway, NSW 2007, Australia (e-mail: pmpoblete@ieee.org; rhcuzmar@uc.cl).

Ricardo P. Aguilera, Dylan Dah-Chuan Lu, and Yam Prasad Siwakoti are with the School of Electrical and Data Engineering, University of Technology Sydney, Broadway, NSW 2007, Australia (e-mail: raguilera@ieee.org; dylan.lu@uts.edu.au; yam.siwakoti@uts.edu.au).

Javier Pereda is with the Department of Electrical Engineering and UC Energy Research Center, Pontificia Universidad Católica de Chile, Santiago 7820436, Chile (e-mail: jepereda@uc.cl).

Abraham M. Alcaide is with the Electronics Department, Universidad de Sevilla, 41092 Sevilla, Spain (e-mail: amarquez@ieee.org).

Pablo Acuna is with the Department of Electrical Engineering, Universidad de Talca, Curicó 3340000, Chile (e-mail: pablo.acuna@utalca.cl).

Color versions of one or more figures in this article are available at https://doi.org/10.1109/TPEL.2024.3472451.

Digital Object Identifier 10.1109/TPEL.2024.3472451

I. Introduction

MULTILEVEL converters (MCs) have been under research and development for decades, receiving wide acceptance in several industrial applications due to their cost-effectiveness in medium- and high-voltage power conversion [1]. Among the different MC topologies, the cascaded H-bridge (CHB) converter is one of the most attractive alternatives given its modular design, fault-tolerant capability, and high output power quality. Suitable applications for the CHB converter include electrical drives [1], static synchronous compensators [2], and battery energy storage systems (BESS) [3].

Several control strategies have been proposed to govern the CHB converter based on the well-known voltage-oriented control schemes [1]. Within these strategies, classical controllers, e.g., proportional–integral regulators designed using the synchronous dq-frame or proportional–resonant (PR) controllers, are often combined with a suitable modulation stage, such as a phase-shifted pulsewidth modulation (PS-PWM) or a level-shift PWM [4], [5], [6], [7]. Nevertheless, due to recent advances in digital control platforms, model predictive control (MPC) schemes have emerged as promising control alternatives for power converters. In general, MPC strategies may outperform standard PWM-based controllers by offering several advantages, such as a simple design process, high dynamic performance, and the ability to include multiple control inputs and outputs, constraints, and nonlinearities [8].

Among the MPC strategies, the finite-control-set MPC (FCS-MPC) is considered the most popular MPC scheme for power converters [8]. In fact, several FCS-MPC strategies have been proposed for the CHB converter [9], [10], [11], [12], [13]. This control strategy avoids an external modulation stage by directly considering the power switches' state (or voltage levels) as input constraints in the optimization problem. Accordingly, all the allowed switching combinations can be evaluated in a cost function, finding the optimal control input at every sampling instant. FCS-MPC strategies are characterized by providing a fast transient response. However, this control scheme faces challenges related to the high computational effort required to evaluate the switching combinations in converters with a large number of submodules (SMs), variable switching frequency, and steady-state error [8].

Indirect MPC schemes for MCs have been proposed to mitigate some of the issues of FCS-MPC strategies while maintaining a fast dynamic response. In indirect MPC approaches, a PWM stage is considered at the converter model instead of directly evaluating the discrete combinations of switch positions. As a consequence, the optimization problem in these MPC strategies is formulated to compute optimal modulating signals or duty cycles. Some examples of recent indirect MPC strategies for the CHB converter, including the modulated MPC (M^2PC) technique and the sequential PS-PWM MPC, can be found in [14], [15], [16], [17], and [18].

One of the major challenges of implementing optimal control strategies for power converters in practical applications is dealing with parameter uncertainty and unaccounted disturbances that might affect the control system [19]. Indeed, the steady-state performance of optimal control methods for the CHB converter is highly dependent on the accuracy of their prediction models [10]. In this sense, parameter mismatch in the converter model, measurement errors, and discretization approximations can drastically deteriorate the performance of these optimal control strategies [9]. Consequently, several methods have been proposed to improve the steady-state performance of optimal control strategies for the CHB converter.

A hybrid FCS-MPC strategy that combines a PR controller working in parallel with the predictive controller is proposed in [13]. The PR controller obtains an average arm voltage reference based on the current tracking error. This reference is used to compute the equivalent switching patterns resulting from feeding the average voltage reference into a conventional PWM stage. Then, these patterns are employed to calculate the switching state reference at the FCS-MPC cost function, improving the steady-state performance and reducing the switching frequency. As the PR controller works in parallel with the FCS-MPC strategy, its settling time must be significantly slower than the sampling frequency, limiting the dynamic response of this steady-state error compensation strategy.

In [10], a PR controller is also combined with an FCS-MPC strategy. Nevertheless, the output voltage of the PR controller is used to compute a compensation voltage, which is included in the CHB converter current prediction model. Following a similar approach in [18] and [20], a sinusoidal steady-state compensation term is proposed to account for the model parameters uncertainty in a modular MC for an M^2PC and a dead-beat current control strategy, respectively. These methods effectively compensate for current tracking errors at the fundamental frequency. However, a unique PR controller per arm cannot properly compensate for higher order voltage harmonic disturbances, which can be introduced into the converter output voltages as a result of measurement errors or low-pass filtering stages in the SM capacitor voltage measurements [20].

A hierarchical multifactorial prediction error correction method is proposed in [9] to improve the CHB converter steady-state performance for an FCS-MPC scheme. This method manipulates the arm current prediction by applying a correction stage derived from an analytic analysis of the potential causes of the steady-state errors. Although this method improves the current total harmonic distortion (THD) under converter parameters mismatch, the experimental results show that it cannot compensate for the third harmonic disturbance component introduced by the SM capacitor voltage ripples in the converter output currents.

From the discussion above, none of the existing methods can compensate for higher order voltage harmonic components that can appear in the arm voltages and deteriorate the steady-state output currents. To overcome this issue, this work proposes a Kalman filter (KF) harmonic compensator strategy to achieve the offset-free optimal control of CHB converters. The proposed KF-based strategy can compensate as many harmonic components as necessary to mitigate the steady-state errors in the CHB converter currents. Moreover, the proposed KF harmonic compensator can be directly integrated with direct and indirect optimal control strategies. The main contributions of this work are summarized as follows.

1) The effect of neglecting the SM capacitor voltage ripples in the CHB converter output voltage is investigated through mathematical analysis. This analysis demonstrates that the SM capacitor voltage ripples can introduce errors in the output voltage, leading to increased voltage harmonic distortion, particularly at the first, third, and fifth harmonic components.
2) An augmented affine state-space model that represents the CHB converter dynamics, including the arm currents and the arm voltage disturbances decomposed into harmonic components, is proposed. This augmented state-space model combined with a state observer allows the estimation of the unaccounted arm voltage disturbances, representing the equivalent voltage drops at the CHB converter arms, related to converter modeling and measurement errors.
3) A harmonic compensator strategy is proposed, considering a steady-state KF as the augmented state observer. Accordingly, guidelines are provided for designing the KF matrices and compensating the control input and the converter prediction model using the estimated voltage disturbances.
4) The performance of the proposed KF harmonic compensator strategy is validated by experiments for three different optimal control strategies under various nonideal operating conditions, including significant errors in the model parameters and assuming constant SM capacitor voltages.

The rest of this article is organized as follows. Section II presents the CHB converter dynamic model and analyzes the effect of the SM capacitor voltage ripples in the converter output voltage. Section III describes the proposed augmented state-space model and the proposed KF harmonic compensator strategy. Section IV presents the experimental validation of the proposed approach. Finally, Section V concludes this article.

II. CHB Converter Model and Standard Optimal Control

Fig. 1 illustrates the CHB converter topology under analysis in this work. This power converter consists of three phase arms in a delta configuration. The arms are formed by the

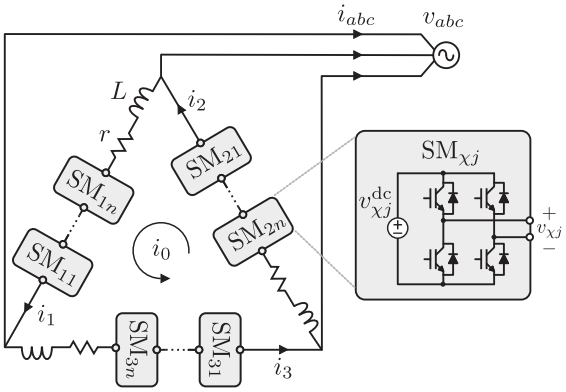

Fig. 1. Delta-connected CHB converter with n power cells.

series connection of n H-bridge SMs (HB-SMs) with an arm filter of inductance L and an arm equivalent resistance r. The dc side of the HB-SMs consists of a floating capacitor, which can be utilized independently or connected to batteries or a dc–dc conversion stage, depending on the application of the CHB converter [1]. The ac side of the HB-SMs has two pairs of power switches, which allows the generation of three different output voltage levels. Each ac terminal of the CHB converter is connected to one phase of the point of common coupling (PCC).

A. Continuous-Time Dynamic Model

To describe the CHB converter current dynamics, the arm currents can be considered as the system state, i.e.,

$$\boldsymbol{x}(t) = \begin{bmatrix} i_1(t) & i_2(t) & i_3(t) \end{bmatrix}^T. \tag{1}$$

Based on the CHB converter topology, as depicted in Fig. 1, the following continuous-time state-space model can be obtained

$$\frac{d\boldsymbol{x}(t)}{dt} = \boldsymbol{A}_c\boldsymbol{x}(t) + \boldsymbol{B}_c\boldsymbol{u}(t) + \boldsymbol{M}_c\boldsymbol{v}_g(t) \tag{2}$$

where is $\boldsymbol{u}(t) = \begin{bmatrix} v_1(t) & v_2(t) & v_3(t) \end{bmatrix}^T$ is the control input formed by the CHB arm output voltages, $v_\chi(t)$, and $\boldsymbol{v}_g(t) = \begin{bmatrix} v_a(t) & v_b(t) & v_c(t) \end{bmatrix}^T$ is the vector containing the PCC voltages. Besides[1]

$$\boldsymbol{A}_c = -\frac{r}{L}\boldsymbol{I}_3,\ \boldsymbol{B}_c = \frac{1}{L}\boldsymbol{I}_3,\ \boldsymbol{M}_c = -\frac{1}{L}\begin{bmatrix} -1 & 1 & 0 \\ 0 & -1 & 1 \\ 1 & 0 & -1 \end{bmatrix}. \tag{3}$$

For a generic n-cell CHB converter arm, the total output voltage can be expressed as the sum of the individual output voltage at each HB-SM, $v_{\chi j}(t)$, as

$$v_\chi(t) = \sum_{j=1}^{n} v_{\chi j}(t) \quad \forall \chi \in \{1, 2, 3\}. \tag{4}$$

[1]Note that $\boldsymbol{I}_n$ refers to the identity matrix of dimension n.

In the delta-connected CHB converter, a circulating current, $i_0(t)$, can be injected into the arm currents without affecting the grid currents. This circulating current allows the control of the interarm power imbalance, achieving different power references at each arm while maintaining balanced ac currents at the converter output [16]. The relationships between the arm currents, the grid currents, and the circulating current can be expressed via

$$\begin{bmatrix} i_a(t) \\ i_b(t) \\ i_0(t) \end{bmatrix} = \boldsymbol{\Psi}\boldsymbol{x}(t), \quad \boldsymbol{\Psi} = \begin{bmatrix} 1 & 0 & -1 \\ -1 & 1 & 0 \\ \frac{1}{3} & \frac{1}{3} & \frac{1}{3} \end{bmatrix} \tag{5}$$

and $i_c(t) = -i_a(t) - i_b(t)$.

B. Discrete-Time Dynamic Model

A discrete-time dynamic model for the CHB converter arm currents is often required to implement optimal control strategies in digital control platforms. In this sense, a discrete-time state-space model can be obtained by applying the zero-order hold (ZOH) discretization to (2), with a sampling period of T_s, leading to

$$\boldsymbol{x}(k+1) = \boldsymbol{A}\boldsymbol{x}(k) + \boldsymbol{B}\boldsymbol{u}(k) + \boldsymbol{M}\boldsymbol{v}_g(k) \tag{6}$$

with

$$\boldsymbol{A} = e^{\boldsymbol{A}_c T_s}, \quad \boldsymbol{B} = \boldsymbol{A}_c^{-1}(\boldsymbol{A} - \boldsymbol{I}_3)\boldsymbol{B}_c \tag{7}$$

$$\boldsymbol{M} = \boldsymbol{A}_c^{-1}(\boldsymbol{A} - \boldsymbol{I}_3)\boldsymbol{M}_c. \tag{8}$$

Furthermore, at each sampling instant, the arm output voltages can be expressed as $v_\chi(k) = \sum_{j=1}^{n} v_{\chi j}(k)$. Consequently, the optimal control strategy chosen to govern the CHB converter defines the range of values allowed for the arm voltages as control inputs. For instance, in FCS-MPC strategies, the control input is often considered as the discrete set of voltage levels that can be obtained at the arm output voltage, i.e., $v_\chi(k) = v_{dc}^\star v_{l\chi}(k)$, with $v_{l\chi}(k) \in \{-n, -n+1, \ldots, 0, \ldots, n-1, n\}$. Conversely, in optimal control strategies that consider a modulation stage, the possible arm output voltages are given by a continuous set of values, defined as $v_\chi(k) \in [-nv_{\text{dc}}^\star, nv_{\text{dc}}^\star]$. In any case, (6) can be used as the converter prediction model in standard optimal control strategies for the CHB converter.

C. Optimal Control Problem and Steady-State Control Input Reference Design

Several standard FCS-MPC and indirect MPC strategies [12], [13], [14], [15], [16] are based on computing the optimal control input, $\boldsymbol{u}^{\text{opt}}(k)$, which minimizes the following cost function:

$$J(k) = \|\boldsymbol{x}(k+1) - \boldsymbol{x}^\star(k+1)\|_2^2 + \lambda_u \|\boldsymbol{u}(k) - \boldsymbol{u}^\star(k)\|_2^2 \tag{9}$$

where $\boldsymbol{u}^\star(k)$ is the required CHB output voltage to maintain the arm currents at the desired steady-state operation conditions. Accordingly, the weighting factor λ_u allows the designer to regulate the controller closed-loop performance [21].

It is important to remark that when the system state approaches its reference, i.e., $\boldsymbol{x}(k) \approx \boldsymbol{x}^\star(k)$, the first term of the cost function (9) is almost zero. As a consequence, the second term

becomes the dominant one, and $\boldsymbol{u}^{\text{opt}}(k)$ tracks $\boldsymbol{u}^{\star}(k)$ in steady state. In this sense, appropriate steady-state reference voltages for the CHB converter arms can be found simply by replacing the system state reference in the dynamic model (6), and solving the equation system for $\boldsymbol{u}(k)$, as follows:

$$\boldsymbol{u}^{\star}(k) = \boldsymbol{B}^{-1}\left(\boldsymbol{x}^{\star}(k+1) - \boldsymbol{A}\boldsymbol{x}^{\star}(k) - \boldsymbol{M}\boldsymbol{v}_g(k)\right). \tag{10}$$

Replacing the model matrices (7) and (8) into (10) yields

$$\boldsymbol{u}^{\star}(k) = r\boldsymbol{x}^{\star}(k) + \frac{r}{\sigma}\left(\boldsymbol{x}^{\star}(k+1) - \boldsymbol{x}^{\star}(k)\right) - L\boldsymbol{M}_c\boldsymbol{v}_g(k) \tag{11}$$

with $\sigma = e^{T_s L/r} - 1$. Moreover, the arm current references can be computed considering the grid current references and the circulating current reference as

$$\boldsymbol{x}^{\star}(k) = \boldsymbol{\Psi}^{-1}\begin{bmatrix} i_a^{\star}(k) & i_b^{\star}(k) & i_0^{\star}(k)\end{bmatrix}^T \tag{12}$$

in which the grid current references can be obtained according to the conventional $p-q$ theory [22], and the circulating current reference can be obtained following the interarm active power balance strategy proposed in [23].

Ideally, (11) should perfectly track the desired steady-state arm current references. However, in practical applications, the steady-state currents can drift from their references due to prediction model errors affecting $\boldsymbol{u}^{\star}(k)$. These errors can originate from model parameter uncertainties, measurement errors, and discretization approximations [9]. Consequently, the proposed KF strategy is designed to compensate for these errors in the CHB converter dynamic model, improving the current predictions and the steady-state control input reference used in standard optimal control schemes.

D. Effect of Unmeasured SM Capacitor Voltage Ripples

It is clear from (11) that parameter errors in r and L, and measurement errors at the PCC voltages, directly affect the steady-state control input reference. Nevertheless, the SM capacitor voltage ripples are also an additional cause for steady-state error, depending on how $\boldsymbol{u}^{\text{opt}}(k)$ is applied to the converter SMs.

In some conventional optimal control strategies for the CHB converter, the SM capacitor voltage ripples are neglected when considering the possible arm output voltage levels [11], [12] or at the modulation stage [17], for FCS-MPC and indirect MPC strategies, respectively. As a result, steady-state errors, proportional to the sum of the SM capacitor voltage ripple amplitudes, appear in the arm output voltages. This issue is analyzed as follows.

Assuming that the arm voltage is divided equally among the SMs and that the average SM capacitor voltages are controlled at their reference, the actual steady-state output voltage of each HB-SM is given by the following:

$$v_{\chi j}(t) = \frac{v_{\chi}^{\star}(t)}{n}\frac{v_{\chi j}^{\text{dc}}(t)}{v_{\text{dc}}^{\star}} \tag{13}$$

with $v_{\chi j}^{\text{dc}}(t)$ being the instantaneous SM capacitor voltage of the SM-χj. Therefore, by replacing (13) into (4), the resulting arm output voltage can be written as follows:

$$v_{\chi}(t) = \frac{v_{\chi}^{\star}(t)}{n v_{\text{dc}}^{\star}}\sum_{j=1}^{n} v_{\chi j}^{\text{dc}}(t). \tag{14}$$

Considering that the balanced SM capacitor voltages are composed of the dc voltage value, and the SM capacitor voltage ripple, i.e., $v_{\chi j}^{\text{dc}}(t) = v_{\text{dc}}^{\star} + \tilde{v}_{\chi j}(t)$, and replacing this expression into (14), leads to

$$v_{\chi}(t) = v_{\chi}^{\star}(k) + \tilde{v}_{\chi}(t), \quad \tilde{v}_{\chi}(t) = \frac{v_{\chi}^{\star}(t)}{n v_{\text{dc}}^{\star}}\sum_{j=1}^{n}\tilde{v}_{\chi j}(t) \tag{15}$$

where $\tilde{v}_{\chi}(t)$ accounts for the arm output voltage error introduced by the sum of the SM capacitor voltage ripples.

Due to the single-phase nature of the CHB converter arms, the SM capacitor voltage ripples inherently contain oscillations at twice the fundamental frequency, ω, and its multiples. However, harmonics higher than fourth order generally can be neglected in the SM capacitor voltage ripples. In this way, the sum of the SM capacitor voltage ripples can be approximated as follows:

$$\sum_{j=1}^{n}\tilde{v}_{\chi j}(t) \approx \tilde{V}_{\chi}^{2\omega}\sin(2\omega t + \phi_{2\omega}) + \tilde{V}_{\chi}^{4\omega}\sin(4\omega t + \phi_{4\omega}). \tag{16}$$

Moreover, replacing (16) into (15) leads to the following approximation for the instantaneous arm output voltage error:

$$\begin{aligned}\tilde{v}_{\chi}(t) \approx\ & m_a\sin(\omega t + \phi_{v\chi})\tilde{V}_{\chi}^{2\omega}\sin(2\omega t + \phi_{2\omega}) \\ & + m_a\sin(\omega t + \phi_{v\chi})\tilde{V}_{\chi}^{4\omega}\sin(4\omega t + \phi_{4\omega})\end{aligned} \tag{17}$$

with $m_a\sin(\omega t + \phi_{v\chi}) = \frac{v_{\chi}^{\star}(t)}{n v_{\text{dc}}^{\star}}$. Finally, expanding (17) by using the sine product to sum trigonometric identity leads to[2]

$$\begin{aligned}\tilde{v}_{\chi}(t) \approx\ & \frac{m_a\tilde{V}_{\chi}^{2\omega}}{2}\left(\cos(\omega t + \phi_{2\omega - v\chi}) - \cos(3\omega t + \phi_{2\omega + v\chi})\right) \\ & + \frac{m_a\tilde{V}_{\chi}^{4\omega}}{2}\left(\cos(3\omega t + \phi_{4\omega - v\chi}) - \cos(5\omega t + \phi_{4\omega + v\chi})\right).\end{aligned} \tag{18}$$

Therefore, neglecting the SM capacitor voltage ripples when applying the CHB optimal control inputs results in a voltage error that can be decomposed into a first, third, and fifth predominant harmonic components. This voltage error propagates through the CHB arm currents, increasing their THD and affecting the steady-state performance of the converter.

III. Proposed KF-Based Steady-State Error Compensation Strategy

This section introduces the proposed KF harmonic compensator for the offset-free optimal control of the CHB converter currents. The proposed KF strategy achieves this objective by estimating the voltage drops in the converter arms, which the standard converter dynamic model (6) cannot describe. Accordingly, the estimated voltages can be used to enhance the

[2]Consider that the notation $\phi_{a\pm b} = \phi_a \pm \phi_b$ is assumed in (18).

steady-state control input reference used by optimal control schemes and to improve the current predictions, eliminating the current steady-state error even if the SM capacitor ripples are not measured.

A. Proposed Augmented State-Space Dynamic Model

The key idea behind the proposed KF steady-state error compensation strategy is to include a model for sinusoidal voltage disturbances composed of several harmonic components, which impact the state dynamics of each arm current. These voltages represent the equivalent voltage drops at the CHB converter arms not considered in the standard converter model (6) due to modeling errors or caused by external disturbances. Then, a steady-state KF is designed to estimate these voltage drops and to predict the arm current values.

As a general case, a sinusoidal voltage harmonic component of constant amplitude and frequency can be expressed in the single-phase $\alpha\beta$-frame as

$$d_h^{\alpha}(t) = d\cos(h\omega t + \phi_h) \tag{19}$$

$$d_h^{\beta}(t) = d\sin(h\omega t + \phi_h) \tag{20}$$

where h denotes the harmonic order, ω is the fundamental frequency, and ϕ_h is its phase, indicating that different voltage harmonic components are not necessarily in phase. Moreover, differentiating the $\alpha\beta$ voltages in (19) and (20), the following dynamic equations that describe this voltage harmonic component can be found:

$$\dot{\boldsymbol{d}}_h^{\alpha\beta}(t) = \begin{bmatrix} 0 & -h\omega \\ h\omega & 0 \end{bmatrix} \boldsymbol{d}_h^{\alpha\beta}(t), \quad \boldsymbol{d}_h^{\alpha\beta}(t) = \begin{bmatrix} d_h^{\alpha}(t) \\ d_h^{\beta}(t) \end{bmatrix}. \tag{21}$$

Accordingly, (21) can be discretized using the ZOH method to obtain a dynamic model of voltage disturbance harmonic components that impact the current of the arm-χ, i.e.,

$$\boldsymbol{d}_{\chi h}^{\alpha\beta}(k+1) = \boldsymbol{\Gamma}_h \boldsymbol{d}_{\chi h}^{\alpha\beta}(k) \tag{22}$$

with

$$\boldsymbol{d}_{\chi h}^{\alpha\beta}(k) = \begin{bmatrix} d_{\chi h}^{\alpha}(k) \\ d_{\chi h}^{\beta}(k) \end{bmatrix}, \ \boldsymbol{\Gamma}_h = \begin{bmatrix} \cos(h\omega T_s) & -\sin(h\omega T_s) \\ \sin(h\omega T_s) & \cos(h\omega T_s) \end{bmatrix}.$$

As analyzed in the previous section, to fully eliminate the steady-state error in the arm currents, a voltage disturbance comprised of a first, third, and fifth harmonic component must be compensated at each arm. Consequently, the following augmented system state is defined:

$$\boldsymbol{x}_a(k) = \begin{bmatrix} \boldsymbol{x}^T(k) & (\boldsymbol{d}^{\alpha\beta}(k))^T \end{bmatrix}^T \in \mathbb{R}^{21\times 1} \tag{23}$$

$$\boldsymbol{d}^{\alpha\beta}(k) = \begin{bmatrix} (\boldsymbol{d}_1^{\alpha\beta}(k))^T & (\boldsymbol{d}_3^{\alpha\beta}(k))^T & (\boldsymbol{d}_5^{\alpha\beta}(k))^T \end{bmatrix}^T \tag{24}$$

where $\boldsymbol{d}_h^{\alpha\beta}(k) = [(\boldsymbol{d}_{1h}^{\alpha\beta}(k))^T \ (\boldsymbol{d}_{2h}^{\alpha\beta}(k))^T \ (\boldsymbol{d}_{3h}^{\alpha\beta}(k))^T]^T \in \mathbb{R}^{6\times 1}$ is the vector containing the respective voltage disturbances of frequency $h\omega$ rad/s that affect each arm. Moreover, considering (23), and the dynamic models (6) and (22), the proposed augmented state-space model that describes the converter and disturbances coupled dynamics can be expressed via

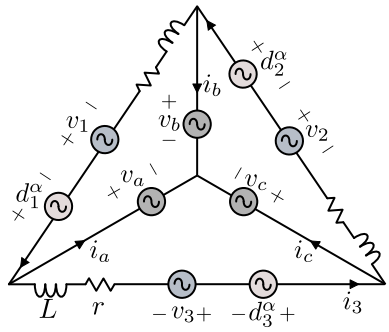

Fig. 2. Equivalent continuous-time circuit diagram of the augmented state-space model for the CHB converter, where $d_{\chi}^{\alpha} = (d_{\chi 1}^{\alpha} + d_{\chi 3}^{\alpha} + d_{\chi 5}^{\alpha})\frac{r\gamma}{L(\gamma-1)}$, $\gamma = e^{T_s r/L}$.

$$\begin{aligned} \boldsymbol{x}_a(k+1) &= \boldsymbol{\mathcal{A}}_a \boldsymbol{x}_a(k) + \boldsymbol{\mathcal{B}}_a \boldsymbol{u}(k) + \boldsymbol{p}(k) \\ \boldsymbol{y}(k) &= \boldsymbol{x}(k) = \boldsymbol{\mathcal{C}}_a \boldsymbol{x}_a(k) \end{aligned} \tag{25}$$

with

$$\boldsymbol{\mathcal{A}}_a = \begin{bmatrix} \boldsymbol{A} & \boldsymbol{D} \\ \boldsymbol{0}_{18\times 3} & \boldsymbol{\Gamma} \end{bmatrix}, \ \boldsymbol{\mathcal{B}}_a = \begin{bmatrix} \boldsymbol{B} \\ \boldsymbol{0}_{18\times 1} \end{bmatrix}, \ \boldsymbol{p}(k) = \begin{bmatrix} \boldsymbol{M}\boldsymbol{v}_g(k) \\ \boldsymbol{0}_{18\times 1} \end{bmatrix}$$

$$\boldsymbol{D} = \begin{bmatrix} \boldsymbol{D}_{\alpha} & \boldsymbol{D}_{\alpha} & \boldsymbol{D}_{\alpha} \end{bmatrix}, \ \boldsymbol{D}_{\alpha} = \begin{bmatrix} 1 & 0 & 0 & 0 & 0 & 0 \\ 0 & 0 & 1 & 0 & 0 & 0 \\ 0 & 0 & 0 & 0 & 1 & 0 \end{bmatrix} \tag{26}$$

$\boldsymbol{\Gamma} = \text{blkdiag}(\boldsymbol{\Gamma}_1, \boldsymbol{\Gamma}_1, \boldsymbol{\Gamma}_1, \boldsymbol{\Gamma}_3, \boldsymbol{\Gamma}_3, \boldsymbol{\Gamma}_3, \boldsymbol{\Gamma}_5, \boldsymbol{\Gamma}_5, \boldsymbol{\Gamma}_5)$, and $\boldsymbol{\mathcal{C}}_a = \begin{bmatrix} \boldsymbol{I}_3 & \boldsymbol{0}_{3\times 18} \end{bmatrix}$. Fig. 2 shows the equivalent circuit representation of the proposed augmented state-space model for the CHB converter topology with disturbances.

Finally, although this work considers the delta-connected CHB converter, the proposed augmented state-space model can be adapted to the star-connected CHB converter by simply updating the converter model matrices $\boldsymbol{A}$, $\boldsymbol{B}$, and $\boldsymbol{M}$ in the augmented model matrices (26).

B. Proposed KF-Based Compensation Strategy

It is important to remark that the proposed augmented affine state-space dynamic model (25) is time-invariant. Furthermore, the observability matrix for this system is full rank. Consequently, any conventional state observer can be designed to estimate the arm voltage disturbances from the arm current measurements. Accordingly, the following state observer dynamic model is considered:

$$\begin{aligned} \hat{\boldsymbol{x}}_a(k+1) &= \boldsymbol{\mathcal{A}}_a \hat{\boldsymbol{x}}_a(k) + \boldsymbol{\mathcal{B}}_a \boldsymbol{u}(k) + \boldsymbol{p}(k) + \boldsymbol{K}_f(\boldsymbol{y}(k) - \hat{\boldsymbol{y}}(k)) \\ \hat{\boldsymbol{y}}(k) &= \boldsymbol{\mathcal{C}}_a \hat{\boldsymbol{x}}_a(k) \end{aligned} \tag{27}$$

where $\boldsymbol{K}_f$ is the observer gain matrix. This matrix must be designed to ensure that the closed-loop observer matrix

$$\boldsymbol{A}_{\text{obs}} = \boldsymbol{\mathcal{A}}_a - \boldsymbol{K}_f \boldsymbol{\mathcal{C}}_a \tag{28}$$

is Schur stable, i.e., all its eigenvalues have a norm strictly less than one. Consequently, this work proposes the application of a steady-state KF [24] to compute the observer gain matrix. In this way, $\boldsymbol{K}_f$ can be obtained offline by solving the following discrete-time algebraic Riccati equation:

$$\boldsymbol{K}_f = \boldsymbol{\mathcal{A}}_a \boldsymbol{P} \boldsymbol{\mathcal{C}}_a^T \left(\boldsymbol{\mathcal{C}}_a \boldsymbol{P} \boldsymbol{\mathcal{C}}_a^T + \boldsymbol{R} \right)^{-1} \tag{29}$$

$$\boldsymbol{P} = \boldsymbol{\mathcal{A}}_a \boldsymbol{P} \boldsymbol{\mathcal{A}}_a^T - \boldsymbol{K}_f \boldsymbol{\mathcal{C}}_a \boldsymbol{P} \boldsymbol{\mathcal{A}}_a^T + \boldsymbol{Q} \tag{30}$$

where $\boldsymbol{P} \in \mathbb{R}^{21\times 21}$ is the steady-state estimate covariance matrix, and $\boldsymbol{Q} \in \mathbb{R}^{21\times 21}$ and $\boldsymbol{R} \in \mathbb{R}^{3\times 3}$ are the process and sensor noise covariance matrices, respectively.

The process noise covariance matrix represents the uncertainty in the dynamic model (23), accounting for the modeling errors that cannot be represented by the proposed voltage harmonic disturbances. Conversely, the sensor noise covariance matrix represents the variability of the current sensor measurements. As the augmented system state is comprised of the arm currents and the sinusoidal voltage disturbances, and considering that the arm currents are the only measured outputs used for the state estimation, the covariance matrices of the proposed KF are defined as follows:

$$\boldsymbol{Q} = \begin{bmatrix} \boldsymbol{I}_3 & \boldsymbol{0}_{3\times 18} \\ \boldsymbol{0}_{18\times 3} & \lambda_q \boldsymbol{I}_{18} \end{bmatrix}, \quad \boldsymbol{R} = \lambda_r \boldsymbol{I}_3 \tag{31}$$

where λ_q and λ_r are positive constants to model the relative uncertainty of the arm voltage disturbance estimates and the current sensors, respectively.

First, in order to design the KF observer, the value of λ_r can be computed by recording a large number of measurements from the current sensors in the experimental setup for a constant input value and then computing the covariance of the dataset. Subsequently, the value of λ_q can be adjusted to achieve the desired closed-loop performance of the state observer.

A small value for λ_q implies that the prediction model is remarkably accurate. As a result, the observer will tend to rely more on the model predictions rather than rapidly adjusting the state estimates of the voltage disturbances based on the arm currents prediction errors. On the contrary, larger values for λ_q imply that the dynamic model is quite uncertain, leading the observer to provide larger corrections to the state estimates based on the estimation errors. Nevertheless, larger values for λ_q can increase the amount of noise propagated from the sensors to the state estimation.

Finally, note that λ_r can also be modified to adjust the observer bandwidth or to avoid numerical rounding errors in the digital control platform when a value close to zero is obtained from the experimental setup measurements. However, it is essential to consider that increasing the value of λ_r makes the observer less aggressive by relying more on the dynamic model, whereas reducing its value diminishes the noise-filtering capabilities of the KF observer.

The predicted voltage disturbance estimates can be extracted from the augmented system state and used to compute the required control input compensation that cancels their effect on the arm output voltages as follows:

$$\hat{\boldsymbol{u}}_d^{\star}(k+1) = \boldsymbol{B}^{-1} \boldsymbol{D} \hat{\boldsymbol{d}}^{\alpha\beta}(k+1) \in \mathbb{R}^3. \tag{32}$$

Adding the control input compensation (32) to (11) leads to the compensated steady-state control input reference, which includes the aggregated modeling errors of the CHB converter. Accordingly, the control input that needs to be provided to the optimal control strategy is given by the following equation:

$$\hat{\boldsymbol{u}}^{\star}(k+1) = \boldsymbol{u}^{\star}(k+1) + \hat{\boldsymbol{u}}_d^{\star}(k+1). \tag{33}$$

Finally, a block diagram that depicts the implementation of the proposed KF strategy is shown in Fig. 3. Note that implementing the proposed KF not only involves using the enhanced steady-state control input reference (33), but also requires feeding the estimated predicted currents to the optimal control, as this state prediction considers the effect of the unmeasured disturbances.[3]

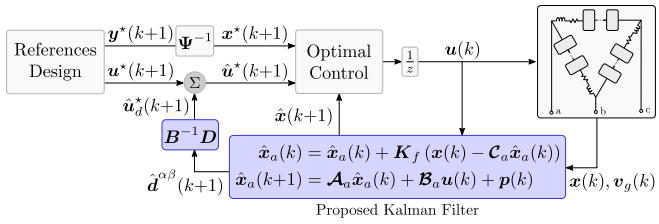

Fig. 3. Block diagram of the proposed KF observer for steady-state error compensation.

Fig. 4. Three-phase CHB-BESS converter prototype.

IV. Experimental Verification

A. Experimental Setup

Experimental results have been carried out to analyze the performance of the proposed KF harmonic compensator. The three-phase CHB converter, as shown in Fig. 4, has been used. This setup consists of a second-life (SL) BESS prototype in which the HB-SMs are directly connected to battery packs.

[3]Note that in FCS-MPC schemes, the proposed model (25) must be used to obtain predictions to $k+2$ for the standard delay compensation technique.

TABLE I
EXPERIMENTAL SETUP SL BATTERY CAPACITIES IN AH

SM	11	12	13	21	22	23	31	32	33
Ah	3.56	4.1	5.53	3.37	3.5	3.84	3.86	4.1	4.0

TABLE II
MAIN PARAMETERS FOR THE EXPERIMENTAL SETUP

Description	Variable	Value
Number HB-SMs	n	9
Arm inductance	L	10 mH
Inductor resistance	r	500 mΩ
SM dc capacitance	C	400 μF
Nominal battery voltage	V_{dc}	80.4 V
Grid voltage (LL-RMS)	V_g, f_0	122.47 V, 50 Hz
Nominal converter power	S_{nom}	1.5 kVA

The SL battery packs are composed of 18 650 Lithium-ion cells, obtained by dismantling discarded electric bike (e-bike) batteries. The cells of each e-bike battery that exhibited a voltage lower than the recommended voltage threshold of 2.75 V were discarded for recycling.

On the other hand, cells with higher voltages were tested and sorted based on their capacity to assemble new SL packs of 24S2P and 24S3P cell configurations. The capacity of the SL battery packs was then tested by doing a complete charge and discharge cycle. A cutoff voltage threshold of 2.75 V for the weakest cell at each pack was set as the terminating condition for the pack capacity tests. The obtained capacities of each pack are given in Table I, and the main parameters of the experimental setup and controller are summarized in Table II.[4]

In addition, the experimental setup includes the grid-simulator REGATRON TC30.528.43-ACS, and an OPAL-RT OP4510 control platform, in which the optimal current control and the proposed KF strategy were implemented in the same CPU core.

B. Steady-State Performance Benchmarking

In order to evaluate the steady-state performance of the proposed KF harmonic compensator, experiments were carried out implementing the observer for three different optimal control schemes: 1) the FCS-MPC [12], 2) the PS-MPC [16], and 3) a standard linear quadratic regulator (LQR) [24]. Moreover, these controllers were also implemented with the PR-based compensation strategy proposed in [10] to compare its performance against the proposed KF harmonic compensator. Table III presents the main parameters for the optimal controllers and their corresponding KF.

The converter parameters were modified to increase the modeling errors for the experiments described in this benchmark analysis. Values of $r = 1\ \Omega$ and $L = 5$ mH were given to the optimal current controllers and observer, introducing parameter errors of 100% and 50% for the arm resistance and inductance, respectively. In addition, the SM capacitor voltages were not

[4]An optimal state-of-charge balancing control scheme for this SL-BESS experimental setup is presented in [25].

TABLE III
OPTIMAL CONTROLLERS AND OBSERVERS PARAMETERS

Description	Variable	FCS-MPC	PS-MPC	LQR
PWM carrier frequency	f_c	–	2 kHz	2 kHz
Sampling frequency	f_s	10 kHz	12 kHz	4 kHz
Controller design	λ_u	10^{-6}	5	10^{-3}
Sensor noise covariance	λ_r	10^{4}	10^{-3}	10^{-3}
Process noise covariance	λ_q	10^{-1}	10^{-3}	10^{-3}

measured for the FCS-MPC and LQR strategies; instead, each SM capacitor voltage was assumed to be equal to 80 V. This assumption was not possible for the PS-MPC, as this strategy requires the SM capacitor voltages for achieving the SM power imbalance needed for the SL-BESS application [15]. However, only the average SM capacitor voltage was passed to the PS-MPC strategy by applying a low-pass filter to the SM capacitor voltage measurements with a cutoff frequency equal to 1 Hz.

The experimental results are displayed in Fig. 5 for the PR-based compensation and in Fig. 6 for the proposed KF strategy. The steady-state compensation techniques were enabled after the first 30 ms of each experimental test. Consequently, the first row of both figures, which show the converter currents tracking, clearly demonstrates that the standard optimal controllers, without a steady-state error compensation strategy, were unable to effectively track the current references due to disturbances caused by model parameter mismatches and SM capacitor voltage ripples. Further details of each experiment are provided in the following sections.

1) FCS-MPC: In this section, two different FCS-MPC strategies are compared. First, the FCS-MPC scheme [10] was implemented. This FCS-MPC strategy utilizes an additional PR controller per arm to enhance the current prediction model and compensate for the steady-state errors. The experimental results for this control scheme are presented in Fig. 5(a)–(e). Second, the FCS-MPC [12] with the proposed KF harmonic compensator was tested, and the obtained experimental results for this strategy are presented in Fig. 6(a)–(e).

The CHB converter currents for each strategy are shown in Figs. 5(a) and 6(a), respectively. Both figures confirm that these steady-state error compensation techniques effectively mitigate the current tracking error at the fundamental frequency. Furthermore, Figs. 5(e) and 6(e) depict the harmonic spectrums of i_a for their respective FCS-MPC strategies. These figures show that before enabling the steady-state error compensation strategies, the FCS-MPC schemes presented the smallest third and fifth disturbance harmonic components for the converter output current, compared with the PS-MPC and the LQR. Accordingly, the FCS-MPC strategies were less sensitive to higher frequency disturbances caused by the SM capacitor voltage ripples regarding the PS-MPC and the LQR.

The proposed KF harmonic compensator provided a better attenuation of the third and fifth voltage harmonic components, reducing the current weighted THD (WTHD) from 0.7% to 0.55% compared to the PR-based strategy. However, the FCS-MPC strategy [10] demonstrated a slightly lower current THD,

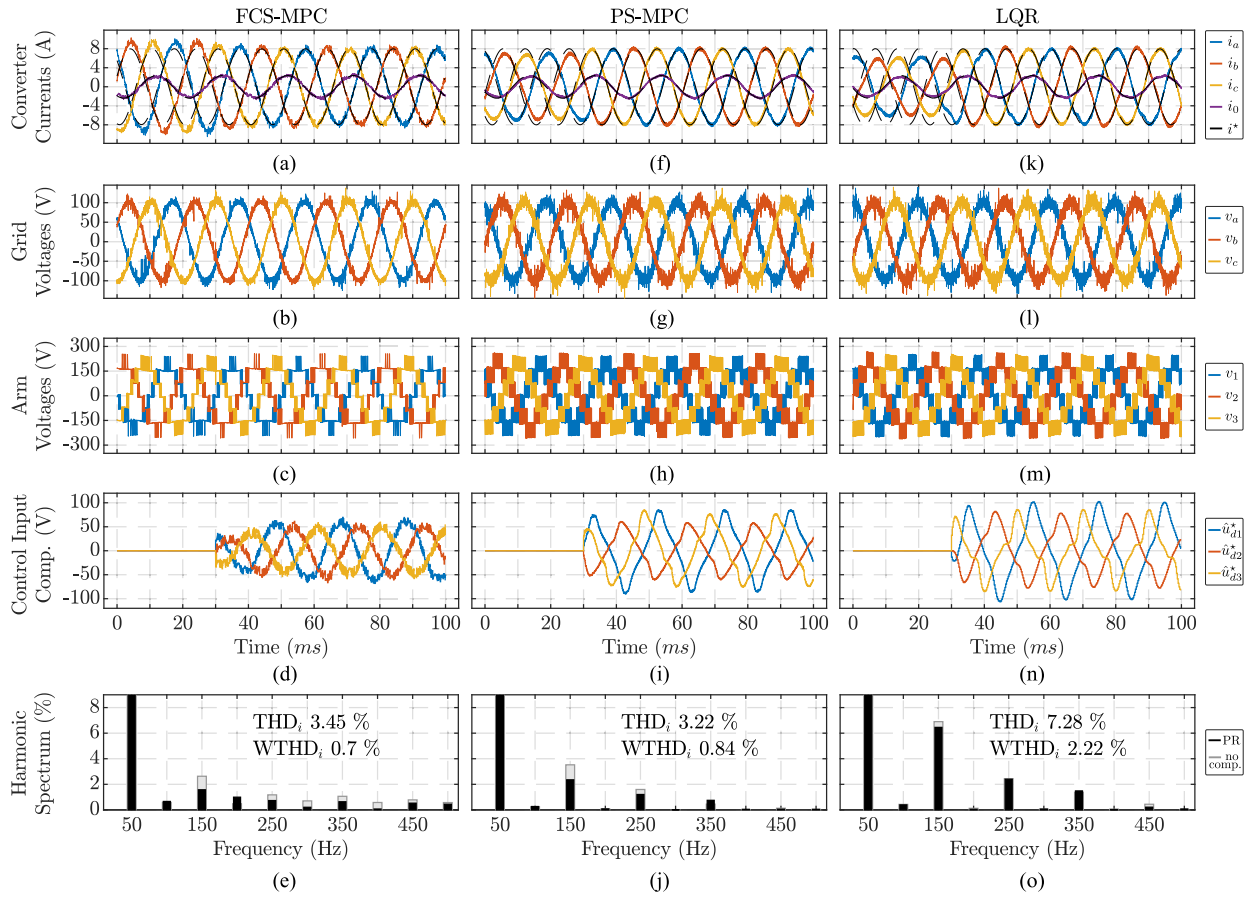

Fig. 5. Experimental results with constant arm power references of $P_1 = P_3 = 500$ W, $P_2 = 200$ W, $Q = 0$ VAr, and the PR-based compensation strategy [10]. (a)–(e) Results for the FCS-MPC. (f)–(j) Results for the PS-MPC. (k)–(o) Results for the LQR. The last row shows the harmonic spectrum of i_a with and without the compensation strategy.

possibly due to its different cost function, which only penalizes current tracking errors, resulting in more aggressive current tracking than in [12].

Based on these results, it is concluded that both PR- and KF-based compensation strategies offer similar steady-state performances for FCS-MPC schemes. In this sense, compensating voltage disturbances of higher order harmonics may not be critical for steady-state error compensation in FCS-MPC strategies with a high sampling frequency, even if the SM capacitor voltages are assumed to be constant.

2) PS-MPC: The experimental results for this M ^{2} PC technique are presented in Fig. 5(f)–(j) and Fig. 6(f)–(j) for the PR- and KF-based compensation strategies, respectively. Despite the high sampling frequency of 12 kHz applied in the PS-MPC, its steady-state performance was severely affected by considering the average SM capacitor voltages instead of the actual SM capacitor voltage measurements to calculate the optimal modulating signals. The current harmonic spectrums shown in Figs. 5(j) and 6(j) exhibit significant harmonic components at 150 and 250 Hz, for the scenarios without compensation strategies. This disadvantage of the PS-MPC compared to the FCS-MPC is caused by the higher weighting factor λ_u, which is required to deal with the higher frequency measurement noise [15]. Therefore, errors in the calculation of $\boldsymbol{u}^\star(k+1)$ are more likely to deteriorate the steady-state current tracking performance under this control scheme.

The PR-based compensation strategy cannot properly mitigate the third and fifth harmonic voltage disturbances. Thus, these disturbances propagate into the arm currents, as shown in Fig. 5(j). On the other hand, the proposed KF harmonic compensator allows the PS-MPC strategy to completely reject the fundamental and higher order voltage disturbances. As a result, the proposed KF harmonic compensator outperforms the PR-based compensation strategy for this optimal control scheme, reducing the output current THD and WHTD in 1.29% and 0.6%, respectively, [see Figs. 5(i) and 6(i)].

3) LQR: An LQR was implemented to obtain the CHB converter arm modulating voltages. These voltages were applied to the HB-SMs by implementing the optimal variable-angle PS-PWM (OVA-PS-PWM) strategy [26] with the sampling technique [27]. This modulation stage is particularly suited for SL-BESS applications since it minimizes the voltage switching harmonic components when different dc voltage and/or power levels are required at each HB-SM. Moreover, this modulation strategy allows the implementation of the current controller at a reduced sampling frequency of 4 kHz while maintaining the same PWM carrier frequency used in the PS-MPC strategy. Nevertheless, the slower sampling frequency and the assumption

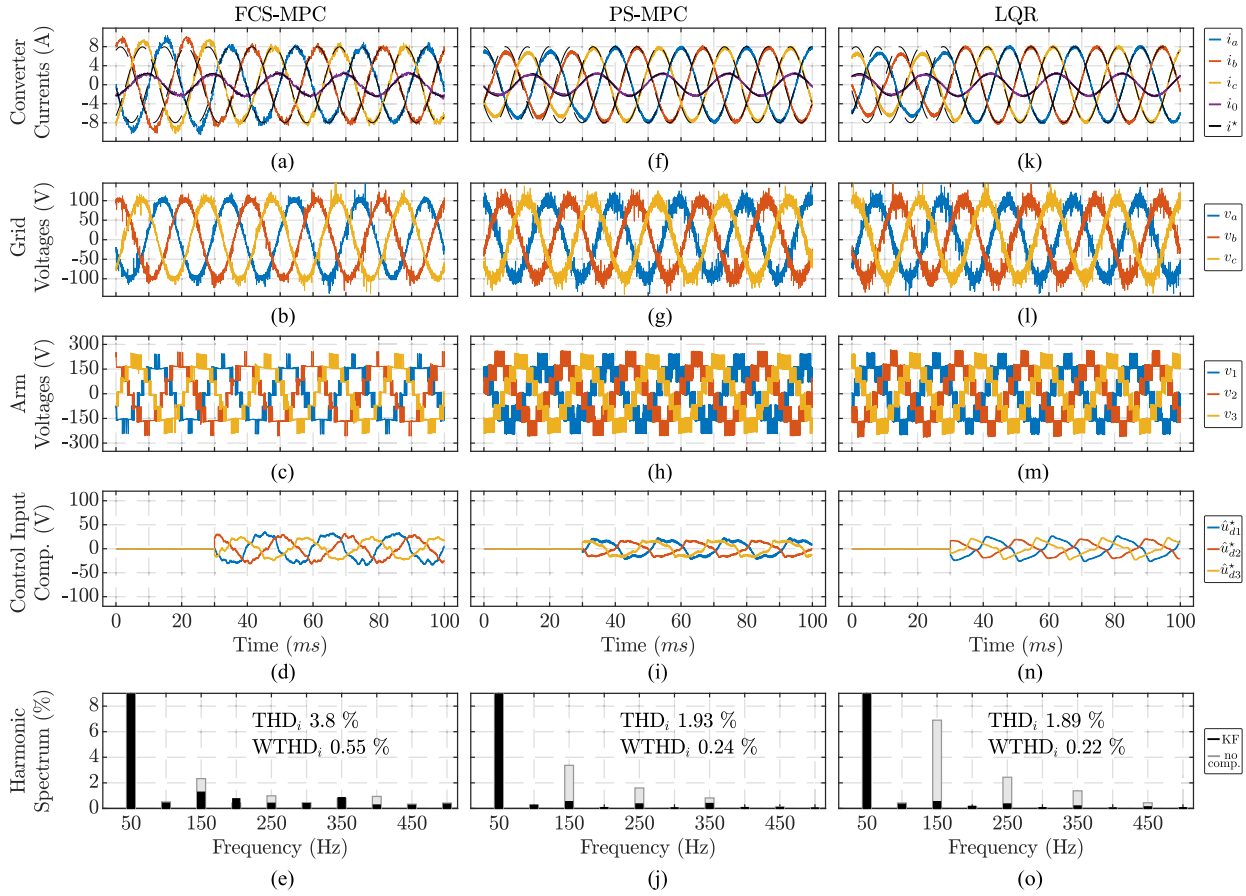

Fig. 6. Experimental results with constant arm power references of $P_1{=}P_3{=}500$W, $P_2{=}200$W, $Q{=}0$VAr, and the proposed KF harmonic compensator. (a)–(e) Results for the FCS-MPC. (f)–(j) Results for the PS-MPC. (k)–(o) Results for the LQR. The last row shows the harmonic spectrum of i_a with and without the compensation strategy.

TABLE IV
THIRD AND FIFTH HARMONIC COMPONENTS OF i_a FOR EACH CONTROL SCHEME AND COMPENSATION TECHNIQUE

Control	FCS-MPC			PS-MPC			LQR		
Compensation	-	PR	KF	-	PR	KF	-	PR	KF
150 Hz (%)	2.63	1.57	1.27	3.52	2.35	0.53	6.90	6.45	0.53
250 Hz (%)	1.18	0.73	0.41	1.60	1.21	0.35	2.44	2.40	0.35

TABLE V
COMPARISON FOR THE OUTPUT CURRENTS THD, RMSE FOR THE STEADY-STATE ARM CURRENT REFERENCES TRACKING, AND COMPUTATIONAL BURDEN

Control System	THD$_i$	RMSE	CPU Load	Execution T.
FCS-MPC-PR	3.45%	0.234	51.43%	51.43 μs
FCS-MPC-KF	3.8%	0.237	51.48%	51.48 μs
PS-MPC-PR	3.22%	0.220	4.89%	4.4 μs
PS-MPC-KF	1.93%	0.185	5.3%	4.42 μs
LQR-OVA-PWM-PR	7.28%	0.269	3.14%	7.86 μs
LQR-OVA-PWM-KF	1.89%	0.123	3.18%	7.95 μs

The CPU load is expressed in the percentage of the sampling period used by the control strategy.

of the SM capacitor voltages being constant values impacted the steady-state performance of the LQR without compensation methods. Indeed, the LQR without steady-state error compensation strategy presented the poorest disturbance rejection for the fundamental, third and fifth voltage harmonics compared to the previous optimal controllers, as shown in Figs. 5(o) and 6(o).

After enabling the steady-state compensation strategies, results similar to those of the PS-MPC were obtained. On the one hand, the LQR with the PR-based compensation strategy proposed in [10] could not compensate for higher order harmonic disturbances propagated into the converter currents. On the other hand, the LQR with the proposed KF harmonic compensator drastically attenuated these voltage disturbances.

Table IV summarizes the magnitude of the third and fifth harmonic components of i_a for each control strategy. These results demonstrate that the proposed KF harmonic compensator provided a superior disturbance rejection at these specific frequencies compared to both the absence of compensation and the PR-based scheme [10] for each optimal control scheme. In addition, Table V summarizes the steady-state performance of each optimal control strategy in terms of output current THD, the root-mean-square error (RMSE) for the arm current references tracking, and also details the computational burden observed on the control platform for each control scheme. This table and Fig. 6(o) show that the smallest RMSE and output current

THD among all the tested control strategies were obtained for the LQR with the proposed KF harmonic compensator and the OVA-PS-PWM stage. However, note from Table IV that the magnitude of the third and fifth harmonic components was the same for the PS-MPC and LQR schemes when combined with the KF strategy.

In this way, the slightly superior performance of the LQR over the PS-MPC was given by the modulation stage. The OVA-PS-PWM provides variable PWM carrier phase-shift angles, improving the THD of the output voltage by minimizing the harmonic components at twice the carrier frequency and its multiples. This modulation strategy outperforms the conventional PS-PWM when the HB-SMs present differences in their dc voltages or ac modulating signals [26], which was the case in the SL-BESS prototype used in this work.

Regarding the computational burden of each control scheme (see Table V), it is essential to highlight that the difference in execution time between implementing the PR-based steady-state error compensation strategy [10] and the proposed KF harmonic compensator was negligible, being less than 1 μs. This outcome is attributed to the reduced computational complexity of the proposed steady-state KF, in which the observer gain matrix is constant and computed offline. Furthermore, the dimension of the augmented model matrices (24) does not depend on the number of SMs, and these matrices are sparse. Thus, the implementation of the state prediction and correction can be optimized to reduce the number of floating-point operations.

It is concluded from the conducted experiments that the proposed KF harmonic compensator can eliminate the CHB converter steady-state current errors under severe parameter uncertainty and SM capacitor voltage measurement errors for direct and indirect MPC schemes. Moreover, the proposed KF harmonic compensator outperforms the existing PR-based solution in modulated optimal control techniques, as it enables a major disturbance rejection for the required higher order voltage harmonic components.

C. Observer Design and Settling Time Sensitivity Analysis

As discussed in Section III-B, to design the proposed KF harmonic compensator, positive values for λ_q and λ_r must be selected. These parameters determine the eigenvalues of $\boldsymbol{A}_{\text{obs}}$, which can provide additional insight into the stability and speed of the observer's response. Accordingly, Fig. 7(a) depicts the location of the closed-loop observer matrix eigenvalues in the z-plane for the KF harmonic compensators implemented for the experimental results. Here, it is clear that these observers are stable, as each eigenvalue of $\boldsymbol{A}_{\text{obs}}$, μ_i, with $i \in \{1, \ldots, 21\}$ presented a magnitude strictly less than one. Moreover, the dominant eigenvalue, $\mu^\star$, which is the one with the largest magnitude, can be used to estimate the observer settling time as $T_{\text{set}} \approx 4/|\sigma_i^\star|$, where $\sigma_i^\star$ is the real part of the equivalent dominant continuous-time eigenvalue[5] [28].

In this way, Fig. 7(b) shows a sensitivity analysis of the observer settling time, given the variation of λ_q and λ_r across a spectrum of values, and considering the CHB converter parameters of the experimental setup given in Table II. The observer response is significantly more sensitive to variations in λ_q than in λ_r. For instance, for a fixed value of $\lambda_q = 10^{-3}$, a substantial increase in λ_r from 10^{-4} to 10 results in only a slight increase in settling time, from 46 to 71 ms. In contrast, with λ_r fixed at 10^{-3}, increasing λ_q from 10^{-4} to 10 reduces the settling time significantly, from 142 to 11 ms. In any case, using the proposed steady-state KF to design the gain matrix ensures that $\boldsymbol{A}_{\text{obs}}$ is Schur stable [24]; thus, the observer design constants can be adjusted to obtain the desired performance without major concerns regarding its closed-loop stability.

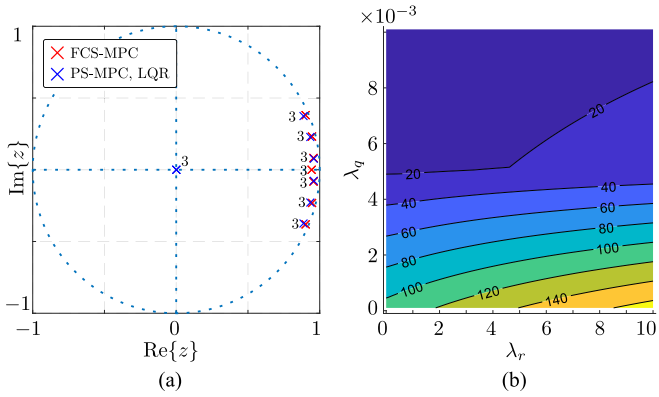

Fig. 7. KF design. (a) $\boldsymbol{A}_{\text{obs}}$ eigenvalues in the z-plane and (b) sensitivity analysis for the observer settling time in milliseconds.

D. Transient Performance

Three transient tests were carried out to assess the dynamic response of the proposed KF strategy. Due to its improved steady-state performance, the LQR current control strategy was implemented in this section. The SM capacitor voltages were assumed to be equal to the average battery voltage for these experiments by applying a low-pass filter to the SM capacitor voltage measurements with a cutoff frequency equal to 1 Hz. The first transient test is given by a circulating current transient to introduce an arm power imbalance. The arm powers were modified from P_1=P_2=P_3=400 W, to P_1=500 W, P_2=200 W, and P_3=500 W; thus, maintaining a constant output power of 1.2 kW. The second and third experiments involved a ramp change in the three-phase active power reference over 10 ms. In particular, the active power was modified from 0 to 1.2 kW in the second test, while a power flow inversion from -1.2 to 1.2 kW was considered in the third test. The results for each experiment are shown in each column of Fig. 8, in which each reference change was introduced at t=30 ms. From these experiments, it is demonstrated that the proposed KF strategy can be used during transient conditions without increasing the overshoot of the current control.

Fig. 9 shows the SM capacitor voltage measurements for the reverse power flow experiment. These SM capacitor voltages presented disparities in their average value and the voltage ripple amplitude, given the differences in the internal resistance of the

[5]A continuous-time eigenvalue can be obtained from a discrete-time eigenvalue as $\mu_i^c = \ln(\mu_i)/T_s$ [28].

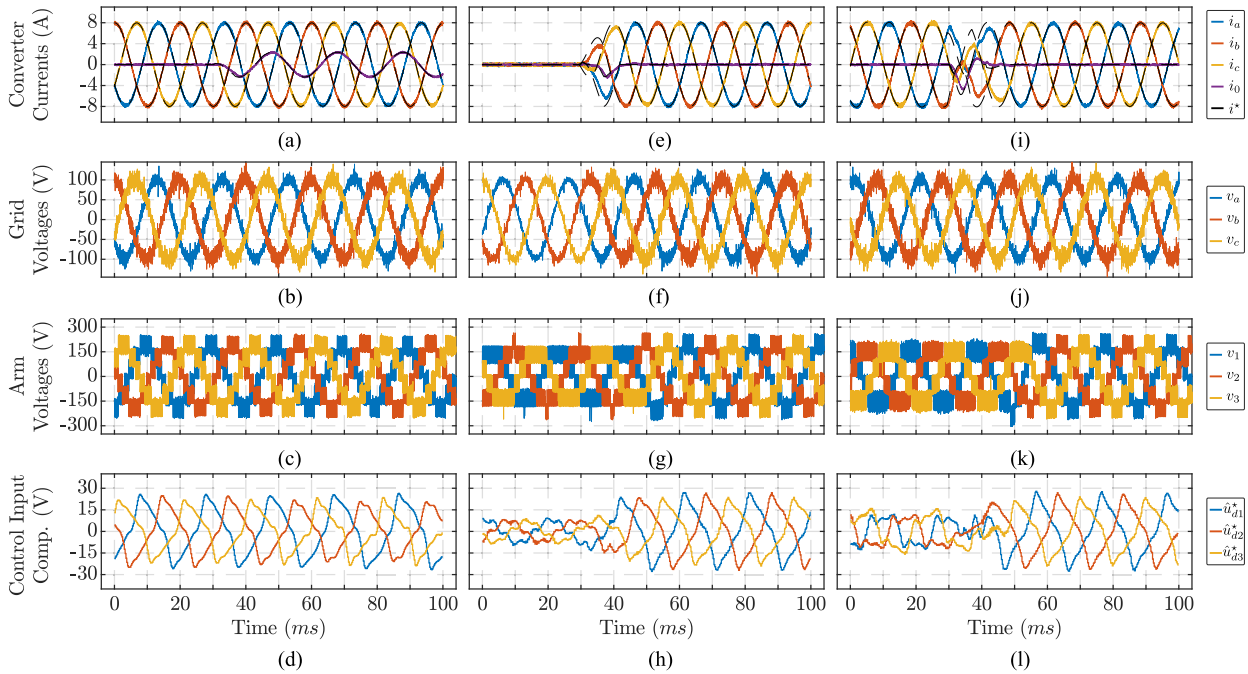

Fig. 8. Experimental results for the proposed KF strategy under transients for an LQR. (a)–(d) Transient response for a circulating current step change. (e)–(h) Active power reference change of 1.2 kW. (j)–(l) Transient reversing the power flow from −1.2 to 1.2 kW.

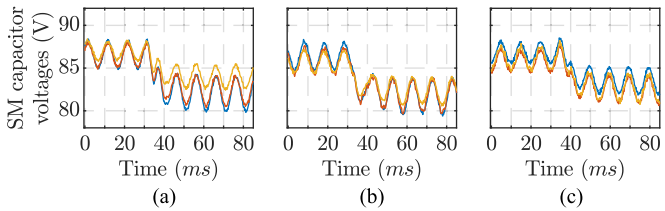

Fig. 9. Experimental results for the SM capacitor voltages for the reverse power flow transient. (a) Voltages arm-1. (b) Voltages arm-2. (c) Voltages arm-3.

SL battery packs. Nevertheless, the voltage differences among SMs did not affect the performance of the proposed KF harmonic compensator. In fact, Fig. 8 shows that the proposed KF strategy allowed the optimal controller to reach the current references without steady-state error, compensating for the harmonic distortion introduced by assuming that the SM capacitor voltages were equal to the average battery voltage.

V. Conclusion

In this article, a KF harmonic compensator to achieve an offset-free optimal control of CHB converters has been proposed. The proposed KF strategy is based on an augmented affine state-space model, which considers sinusoidal voltage disturbances of different harmonic components that affect the arm currents dynamics. These disturbances represent the equivalent voltage drops at the converter arms caused by modeling errors. In this way, the proposed KF harmonic compensator strategy estimates these voltage disturbances and improves the converter steady-state current tracking by providing a corrected steady-state control input reference and enhancing arm current predictions.

Experimental results for a three-phase CHB-BESS prototype have verified the effectiveness of the proposed KF harmonic compensator, tested with the FCS-MPC, PS-MPC, and LQR control strategies. These results show that the proposed KF strategy can completely eliminate the steady-state error introduced by significant model parameters and SM capacitor voltage measurement errors.

The experimental results showed that if the SM capacitor voltages are assumed to be constant, the proposed KF harmonic compensator significantly outperforms the steady-state compensation technique [10], which combines an optimal control strategy with a PR controller for modulated optimal control strategies. However, both the steady-state error compensation strategies presented similar performances for the FCS-MPC schemes, indicating that the FCS-MPC is less sensitive to higher order harmonic disturbances in the SM capacitor voltage ripples compared to the PS-MPC and LQR strategies.

Therefore, the proposed KF harmonic compensator strategy offers a suitable solution for improving the steady-state performance of optimal controllers in scenarios with model parameter uncertainty. Moreover, it is important to remark that it can be easily integrated into existing optimal control schemes for CHB converters, with and without a PWM stage. In addition, it has the potential to reduce the converter measurement hardware requirements for some CHB converter applications in which the SM capacitor voltages are regulated by external power sources. In this sense, the proposed KF harmonic compensator can be particularly advantageous for BESS and electrical drive applications.

REFERENCES

[1] J. I. Leon, S. Vazquez, and L. G. Franquelo, "Multilevel converters: Control and modulation techniques for their operation and industrial applications," *Proc. IEEE*, vol. 105, no. 11, pp. 2066–2081, Nov. 2017.

[2] Y. Koyama, Y. Nakazawa, H. Mochikawa, A. Kuzumaki, K. Sano, and N. Okada, "A transformerless 6.6-kv STATCOM based on hybrid cascade multilevel converter using SiC devices," *IEEE Trans. Power Electron.*, vol. 33, no. 9, pp. 7411–7423, Sep. 2018.

[3] M. Stecca, L. R. Elizondo, T. B. Soeiro, P. Bauer, and P. Palensky, "A comprehensive review of the integration of battery energy storage systems into distribution networks," *IEEE Open J. Ind. Electron. Soc.*, vol. 1, no. 1, pp. 46–65, Sep. 2020.

[4] M. Hagiwara, R. Maeda, and H. Akagi, "Negative-sequence reactive-power control by a PWM STATCOM based on a modular multilevel cascade converter (MMCC-SDBC)," *IEEE Trans. Ind. Appl.*, vol. 48, no. 2, pp. 720–729, Mar./Apr. 2012.

[5] G. Farivar, B. Hredzak, and V. G. Agelidis, "Decoupled control system for cascaded h-bridge multilevel converter based STATCOM," *IEEE Trans. Ind. Electron.*, vol. 63, no. 1, pp. 322–331, Jan. 2016.

[6] P. Sochor and H. Akagi, "Theoretical and experimental comparison between phase-shifted PWM and level-shifted PWM in a modular multilevel SDBC inverter for utility-scale photovoltaic applications," *IEEE Trans. Ind. Appl.*, vol. 53, no. 5, pp. 4695–4707, Sep./Oct. 2017.

[7] V. G. Monopoli et al., "Applications and modulation methods for modular converters enabling unequal cell power sharing: Carrier variable-angle phase-displacement modulation methods," *IEEE Ind. Electron. Mag.*, vol. 16, no. 1, pp. 19–30, Mar. 2022.

[8] I. Harbi et al., "Model-predictive control of multilevel inverters: Challenges, recent advances, and trends," *IEEE Trans. Power Electron*, vol. 38, no. 9, pp. 10845–10868, Sep. 2023.

[9] Y. Wang, F. Liu, S. Chen, G. Shen, and Q.-G. Wang, "Prediction errors analysis and correction on FCS-MPC for the cascaded H-bridge multilevel inverter," *IEEE Trans. Ind. Electron.*, vol. 69, no. 8, pp. 8264–8273, Aug. 2022.

[10] C. R. Baier, R. O. Ramirez, E. I. Marciel, J. C. Hernández, P. E. Melín, and E. E. Espinosa, "FCS-MPC without steady-state error applied to a grid-connected cascaded H-bridge multilevel inverter," *IEEE Trans. Power Electron.*, vol. 36, no. 10, pp. 11785–11799, Oct. 2021.

[11] R. Baidya, R. P. Aguilera, P. Acuña, S. Vazquez, and H. D. T. Mouton, "Multistep model predictive control for cascaded H-bridge inverters: Formulation and analysis," *IEEE Trans. Power Electron.*, vol. 33, no. 1, pp. 876–886, Jan. 2018.

[12] R. P. Aguilera et al., "Predictive control of cascaded H-bridge converters under unbalanced power generation," *IEEE Trans. Ind. Electron.*, vol. 64, no. 1, pp. 4–13, Jan. 2017.

[13] R. O. Ramírez, C. R. Baier, F. Villarroel, J. R. Espinoza, J. Pou, and J. Rodríguez, "A hybrid FCS-MPC with low and fixed switching frequency without steady-state error applied to a grid-connected CHB inverter," *IEEE Access*, vol. 8, pp. 223637–223651, 2020.

[14] S. Neira, P. Poblete, R. Cuzmar, J. Pereda, and R. P. Aguilera, "Sequential phase-shifted model predictive control for a multilevel converter with integrated battery energy storage," in *Proc. 2020 IEEE 11th Int. Symp. Power Electron. Distrib. Gener. Syst.*, 2020, pp. 29–34.

[15] R. H. Cuzmar, J. Pereda, and R. P. Aguilera, "Phase-shifted model predictive control to achieve power balance of CHB converters for large-scale photovoltaic integration," *IEEE Trans. Ind. Electron.*, vol. 68, no. 10, pp. 9619–9629, Oct. 2021.

[16] R. H. Cuzmar, P. Poblete, R. P. Aguilera, J. Pereda, and D. D.-C. Lu, "Power balance of a delta-connected CHB converter with MPC for photovoltaic systems," in *Proc. 2023 IEEE Int. Future Energy Electron. Conf.*, 2023, pp. 305–310.

[17] Q. Xiao et al., "Modulated model predictive control for multilevel cascaded H-bridge converter-based static synchronous compensator," *IEEE Trans. Ind. Electron.*, vol. 69, no. 2, pp. 1091–1102, Feb. 2022.

[18] Q. Xiao et al., "Space-vector-equalized predictive current control scheme for the modular multilevel converter with improved steady-state performance," *IEEE Trans. Ind. Electron.*, vol. 70, no. 7, pp. 6470–6481, Jul. 2023.

[19] R. P. Aguilera, P. Lezana, and D. E. Quevedo, "Finite-control-set model predictive control with improved steady-state performance," *IEEE Trans. Ind. Inform.*, vol. 9, no. 2, pp. 658–667, May 2013.

[20] J. Wang, Y. Tang, P. Lin, X. Liu, and J. Pou, "Deadbeat predictive current control for modular multilevel converters with enhanced steady-state performance and stability," *IEEE Trans. Power Electron.*, vol. 35, no. 7, pp. 6878–6894, Jul. 2020.

[21] R. P. Aguilera and D. E. Quevedo, "Predictive control of power converters: Designs with guaranteed performance," *IEEE Trans. Ind. Inform.*, vol. 11, no. 1, pp. 53–63, Feb. 2015.

[22] H. Akagi, E. H. Watanabe, and M. Aredes, *Instantaneous Power Theory and Applications to Power Conditioning*. Hoboken, NJ, USA: Wiley, 2017.

[23] Y. Yu, G. Konstantinou, C. D. Townsend, R. P. Aguilera, and V. G. Agelidis, "Delta-connected cascaded H-bridge multilevel converters for large-scale photovoltaic grid integration," *IEEE Trans. Ind. Electron.*, vol. 64, no. 11, pp. 8877–8886, Nov. 2017.

[24] G. C. Goodwin, S. F. Graebe, and M. E. Salgado, *Control System Design*, 1st ed. Hoboken, NJ, USA: Prentice Hall, 2000.

[25] P. Poblete et al., "Dual-stage MPC for SoC balancing in second-life battery energy storage systems based on delta-connected cascaded H-bridge converters," *IEEE Trans. Power Electron.*, early access, Sep. 18, 2024, doi: 10.1109/TPEL.2024.3461749.

[26] P. Poblete et al., "Predictive optimal variable-angle PS-PWM strategy for cascaded H-bridge converters," *IEEE Trans. Ind. Electron.*, vol. 71, no. 11, pp. 13556–13566, Nov. 2024.

[27] A. M. Alcaide et al., "Generalized feed-forward sampling method for multilevel cascaded h-bridge converters," *IEEE Trans. Ind. Electron.*, vol. 71, no. 8, pp. 8259–8267, Aug. 2024.

[28] R. C. Dorf and R. H. Bishop, *Modern Control Systems*, 9th ed. Hoboken, NJ, USA: Prentice-Hall, 2000.

Pablo Poblete (Member, IEEE) received the B.Sc. degree with highest honors in electrical engineering from the Pontificia Universidad Católica de Chile (PUC), Santiago, Chile, in 2018, and the Ph.D. degree in electrical engineering from PUC and the University of Technology Sydney (UTS), Ultimo, NSW, Australia, in 2024.

From 2017 to 2024, he was a Member with Power and Energy Conversion Laboratory, PUC. Since 2024, he has been with the School of Electrical and Data Engineering, UTS, where he currently holds a Research Assistant and Casual Academic position. His research interests include control in power electronics, second-life battery energy storage systems, and multilevel converters.

Ricardo P. Aguilera (Member, IEEE) received the B.Sc. degree in electrical engineering from the Universidad de Antofagasta, Antofagasta, Chile, the M.Sc. degree in electronics engineering from the Universidad Tecnica Federico Santa Maria, Valparaíso, Chile, and the Ph.D. degree in electrical engineering from The University of Newcastle (UoN), Newcastle, NSW, Australia, in 2003, 2007, and 2012, respectively.

From 2012 to 2013, he was a Research Academic with UoN, where he was a part of the Centre for Complex Dynamic Systems and Control. From 2014 to 2016, he was a Senior Research Associate with The University of New South Wales, Sydney, NSW, Australia, where he was a part of the Australian Energy Research Institute. Since September 2016, he has been with the School of Electrical and Data Engineering, University of Technology Sydney, Sydney, where he currently holds an Associate Professor position. His research interests include theoretical and practical aspects on model predictive control with application to power electronics, renewable energy integration, and microgrids.

Javier Pereda (Senior Member, IEEE) received the B.Sc. (Eng.) degree with highest honors in electrical engineering and the M.Sc. and Ph.D. degrees in electrical engineering from Pontificia Universidad Católica de Chile, Santiago, Chile, in 2009 and 2013, respectively.

In 2013, he joined the Electrical Department, Pontificia Universidad Católica de Chile, where he is currently an Associate Professor. From 2014 to 2016, he was an Associate Research with the Control and Power Group, Department of Electrical and Electronic Engineering, Imperial College London, London, U.K. He is an Associate Researcher with UC Energy Research Center, Santiago, and the Solar Energy Research Center (SERC Chile). He is the Principal Investigator with the Electric Vehicle Laboratory and the Power and Energy Conversion Laboratory (PEClab), Pontificia Universidad Católica de Chile. His research interests include power electronics and control applied to electric vehicles, energy storage, ac and dc electric networks, renewable energy, multilevel converters, industrial applications, and motor drives.

Rodrigo H. Cuzmar received the B.Sc. (Eng.) degree with honors in electrical engineering and the M.Sc. degree in electrical engineering from Pontificia Universidad Católica de Chile (PUC), Santiago, Chile, in 2017 and 2020, respectively. He is currently working toward the Ph.D. degree in electrical engineering in a double-degree program with PUC and University of Technology Sydney, Sydney, NSW, Australia.

Since 2017, he has been a part of Power and Energy Conversion Laboratory (PEClab), PUC. His current research interests include predictive control of power converters applied to energy storage, solar energy conversion, and industrial applications.

Abraham M. Alcaide (Member, IEEE) was born in Huelva, Spain, in 1985. He received the B.S., M.S., and Ph.D. degrees in telecommunications engineering from Universidad de Sevilla (US), Seville, Spain, in 2014, 2016, and 2019, respectively.

His research interests include advanced modulation techniques, multilevel converters, modular converters, model-based predictive control of power converters and drives, renewable energy sources, thermal modeling of power converters, and power device lifetime extension. He is the coauthor of more than 50 journal articles and participated in more than 20 R&D projects.

Dr. Alcaide was the recipient as the coauthor of the 2015, 2021, and 2023 Best Paper Award of *IEEE Industrial Electronics Magazine*.

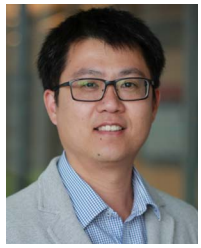

Dylan Dah-Chuan Lu (Senior Member, IEEE) received the Ph.D. degree in electronic and information engineering from the Hong Kong Polytechnic University, Hong Kong, in 2004.

In 2003, he joined PowerELab Ltd. as a Senior Design Engineer, where he was responsible for industrial switching power supply projects. From 2006 to 2016, he was a full-time Faculty Member with the University of Sydney, Sydney, NSW, Australia. In July 2016, he joined the University of Technology Sydney, where he is currently a Professor and the Head of Discipline of Electrical Power and Energy Systems with the School of Electrical and Data Engineering. His current research interests and publications include efficient, cost-effective, and reliable power conversion for renewable energy sources, energy storage systems, and microgrids.

Dr. Lu was the Chair of the Joint Chapter IAS/IES/PELS (IEEE New South Wales Section) from 2020 to 2023. He is currently an Associate Editor for IEEE TRANSACTIONS ON INDUSTRIAL ELECTRONICS and IEEE JOURNAL OF EMERGING AND SELECTED TOPICS IN POWER ELECTRONICS.

Yam Prasad Siwakoti (Senior Member, IEEE) received the B.Tech. degree in electrical engineering from the National Institute of Technology, Hamirpur, India, in 2005, the master's degree in electrical power engineering from the Norwegian University of Science and Technology, Trondheim, Norway, and Kathmandu University, Dhulikhel, Nepal, in 2010, and the Ph.D. degree in electronic engineering from Macquarie University, Sydney, NSW, Australia, in 2014.

From 2014–2016, he was a Postdoctoral Fellow with the Department of Energy Technology, Aalborg University, Copenhagen, Denmark. In 2023, he was a Visiting Professor with the Department of Engineering Science, University of Oxford, Oxford, U.K. In 2018 and 2023, he was also a Visiting Scientist with the Fraunhofer Institute for Solar Energy Systems, Freiburg, Germany. His research has been recognized by a series of awards and recognition, including the most prestigious Friedrich Wilhelm Bessel Research Award from the Alexander von Humboldt Foundation, Germany, in 2022, and the Green Talent Award from the Federal Ministry of Education and Research, Germany, in 2016. He was also recognized as a "Field Leader" in power engineering by The Australian's annual Research Magazine, in 2023. He is currently an Associate Professor with the University of Technology Sydney, Ultimo, NSW, Australia.

Dr. Siwakoti is also an Associate Editor for IEEE TRANSACTIONS ON POWER ELECTRONICS, IEEE TRANSACTIONS ON INDUSTRIAL ELECTRONICS, and IEEE JOURNAL OF EMERGING AND SELECTED TOPICS IN POWER ELECTRONICS.

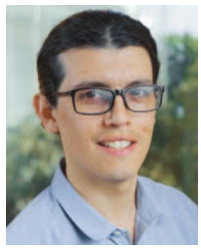

Pablo Acuna (Member, IEEE) received the B.Sc. degree in electronics engineering, the B.Eng. degree in electronics engineering, and the Ph.D. degree in electrical engineering from the University of Concepción, Concepción, Chile, in 2004, 2007, and 2013, respectively.

From 2014 to 2017, he was a Research Associate with UNSW Sydney, Sydney, NSW, Australia. From 2018 to 2019, he was a Lecturer with RMIT University, Melbourne, VIC, Australia. He is currently an Associate Professor with Universidad de Talca, Talca, Chile. His research interests include high-power conversion systems and their applications in industry, transportation, and utility.